



ELSEVIER

Available online at www.sciencedirect.com

SCIENCE @ DIRECT®

Computers & Fluids 34 (2005) 1223–1238

**computers
&
fluids**

www.elsevier.com/locate/compfluid

Numerical simulation of the transient flow behaviour in chemical reactors using a penalisation method

Kai Schneider *

*Laboratoire de Modélisation et Simulation Numérique en Mécanique UMR 6181,
CNRS et Universités d'Aix-Marseille, and
Centre de Mathématiques et d'Informatique, Université de Provence 39, rue F. Joliot-Curie,
13453 Marseille Cedex 13, France*

Received 20 November 2002; received in revised form 18 May 2004; accepted 18 September 2004
Available online 28 January 2005

Abstract

We present a numerical scheme to study the transient flow behaviour in complex geometries. The Navier–Stokes equations are discretized with a high-resolution Fourier pseudo-spectral discretization with adaptive time-stepping. Using a penalisation technique solid boundaries of arbitrary shape can be easily taken into account. As application we present different simulations of unsteady flows, typically encountered in chemical reactors. We study transitional flows in tube bundles (arrays of cylinders and squares) for different Reynolds numbers and angles of incidence and a channel flow with an obstacle.

© 2004 Elsevier Ltd. All rights reserved.

1. Introduction

The numerical simulation of turbulent flows in complex geometries is one of the main challenges in computational fluid dynamics (CFD). A crucial point plays hereby the grid generation and the turbulence modelling near the wall, which is primordial importance for the

* Address: Centre de Mathématiques et d'Informatique, Université de Provence, 39 rue F. Joliot-Curie, 13453 Marseille Cedex 13, France. Tel.: +33 4 91 11 85 29; fax: +33 4 91 11 35 02.

E-mail address: kschneid@cmi.univ-mrs.fr

prediction and the control of the flow. Many industrial CFD applications are dealing with such complex problems, in particular for the design and optimization of chemical reactors, e.g. to predict drag, lift, heat transfer coefficients in heat exchangers, especially in the unsteady regime.

So far different approaches to deal with complex geometries in CFD have been developed. Body fitted coordinates require the numerical scheme to be adapted to the geometry [7]. Coordinate transform techniques allow to use solvers developed for simple geometries, but they are restricted to relatively simple geometries. Fictitious domain approaches, see for example [11], surface [15,12,22] and volume penalisation methods [2] modify the governing equations by adding supplementary terms. These imbedding methods solve the resulting equations on a simple geometry for which fast solvers are available.

In the present paper we review such a recent approach, the volume penalisation method, to model flows in complex geometries and show different applications relevant for chemical engineering. The volume penalisation method has been originally introduced by Arquis and Caltagirone [2] for flows in porous media, in [1] the approach was extended to model obstacles in viscous flows. The physical idea is to model walls or solid obstacles as a porous medium whose permeability η tends to zero. The Navier–Stokes equations are modified accordingly by adding a Darcy term. Fluid regions are considered as completely permeable, while regions where walls or obstacles are present as perfectly impermeable. The geometry of the flow can therefore simply be taken into account using a spatially varying permeability coefficient, which enables an easy practical implementation of the method and allows furthermore obstacles and walls changing in time and interacting with the fluid. A mathematical theory proving convergence of this physically based approach has been given by Angot et al. [1]. The penalisation method has been applied in the context of low order methods (finite difference/volume scheme, e.g. [14,1], with pseudo-spectral methods, e.g. [8,19,13] and recently also with adaptive wavelet methods [10,20]. The latter scheme automatically adapts the spatial grid not only to the evolution of the flow, but also to the geometry of walls or bluff bodies [20].

The paper is organised as follows: First we present the governing equations together with the penalisation method. Then we present a pseudo-spectral method with adaptive time stepping to solve the penalised Navier–Stokes equations numerically. In the Results' section we study several applications of unsteady transitional flows in arrays of cylinders, as encountered in heat exchangers, in array of squares, typically used for static mixers. We discuss the drag and lift coefficients the different geometries and the influence of the angles of attack of the flow. We also present a simulation of a flow in a channel with an obstacle. Finally, we give some conclusions and perspectives for turbulence modelling.

2. The penalisation method

In this section we present the governing equations together with the penalisation technique. We consider a viscous incompressible fluid governed by the Navier–Stokes equations in the fluid region and imposing no-slip boundary conditions on the walls. In primitive variables we have the following equations:

$$\partial_t \vec{u} + \vec{u} \cdot \nabla \vec{u} + \frac{1}{\rho} \nabla p - \nu \nabla^2 \vec{u} = \vec{f} \tag{1}$$

$$\nabla \cdot \vec{u} = 0 \tag{2}$$

where $\vec{u}(\vec{x}, t)$ is the velocity, $p(\vec{x}, t)$ the pressure, \vec{f} the external forces per mass and ν the kinematic viscosity. In the following the density ρ is assumed to be 1 and the external forces \vec{f} to be 0.

The penalisation technique is based on the physical idea to model solid walls or obstacles as porous media whose permeability η is tending to zero [2]. The geometry is described by a mask function $\chi(\vec{x})$ which is 1 inside the solid regions and 0 elsewhere. Hence, the penalisation method can also take into account obstacles with time-varying shape by simply introducing a time-dependent mask function. The above Navier–Stokes equations (2) are modified by adding a supplementary term containing the mask function. For $\eta \rightarrow 0$ the flow evolution is governed by the Navier–Stokes equations in the fluid regions, and by Darcy’s law, i.e. the velocity is proportional to the pressure gradient, in the solid regions where obstacles or walls are present. For the ‘penalised’ velocity \vec{u}_η we obtain

$$\partial_t \vec{u}_\eta + \vec{u}_\eta \cdot \nabla \vec{u}_\eta + \nabla p_\eta - \nu \nabla^2 \vec{u}_\eta + \frac{1}{\eta} \chi_{\Omega_s} \vec{u}_\eta = 0 \tag{3}$$

with the mask function

$$\chi_{\Omega_s}(\vec{x}) = \begin{cases} 1 & \text{for } \vec{x} \in \vec{\Omega}_s \\ 0 & \text{elsewhere} \end{cases} \tag{4}$$

and where Ω_s denotes the ensemble of solid obstacles. In [1] it has been shown rigorously that the above equations converge towards the Navier–Stokes equations with no-slip boundary conditions, with order $\eta^{3/4}$ inside the obstacle and with order $\eta^{1/4}$ elsewhere, in the limit when η tends to zero. In numerical simulations an improved convergence of order η has been reported [1,13].

The resulting forces \vec{F} on the obstacle can be computed by integrating the penalised velocity over the obstacle’s volume [1]:

$$\vec{F} = \lim_{\eta \rightarrow 0} \int_{\Omega_s} \nabla p_\eta \, dx = - \lim_{\eta \rightarrow 0} \frac{1}{\eta} \int_{\Omega_s} \vec{u}_\eta \, dx = \int_{\partial \Omega_s} \sigma(\vec{u}, p) \cdot \vec{n}_f \, d\gamma \tag{5}$$

where Ω_s is the obstacle’s volume, $\partial \Omega_s$ its boundary, \vec{n} its outer normal and $\sigma(\vec{u}, p) = \frac{1}{2\nu} (\nabla \vec{u} + (\nabla \vec{u})^t) - pI$ the stress tensor. Hence the lift and drag forces on the obstacle, i.e. forces parallel and perpendicular to the free-stream velocity of the flow, are easy to compute as volume integrals instead of contour integrals.

For the application of the penalisation method to two-dimensional flows we prefer the vorticity–velocity formulation which results in a scalar valued equation. Therefore, we compute the curl of Eq. (3), and we get

$$\partial_t \omega_\eta + (\vec{u}_\eta + \vec{V}_\infty) \cdot \nabla \omega_\eta - \nu \nabla^2 \omega_\eta + \nabla \times \left(\frac{1}{\eta} \chi_{\Omega_s} \vec{u}_\eta \right) = 0 \tag{6}$$

where $\omega = \nabla \times \vec{u}$ is the vorticity and \vec{V}_∞ is the free-stream velocity, defined as $\lim_{|\vec{x}| \rightarrow \infty} \vec{u}(\vec{x}) = \vec{V}_\infty$.

Using the vector identity $\nabla \times (f \nabla^\perp \Psi) = \nabla \cdot (f \nabla \Psi)$ it follows

$$\partial_t \omega_\eta + (\vec{u}_\eta + \vec{V}_\infty) \cdot \nabla \omega_\eta - \nu \nabla^2 \omega_\eta + \frac{1}{\eta} \nabla \cdot (\chi_{\Omega_s} \nabla \Psi) = 0 \quad (7)$$

with the stream function Ψ , satisfying $\nabla^2 \Psi = \omega$ and $\nabla^\perp \Psi = (-\partial_y \Psi, \partial_x \Psi) = \vec{u}$.

3. Pseudo-spectral implementation with adaptive time-stepping

For the numerical solution of the penalised Navier–Stokes equations in vorticity–velocity formulation (6) we discretize the equations in space and time. For the former we use a classical Fourier-pseudo-spectral method on a rectangular periodic domain. For the latter we developed a variable time-stepping semi-implicit scheme with exact time integration for the diffusion term, $\nabla^2 \omega$, and a second-order Adams–Bashforth scheme for the convective and the penalisation term.

3.1. Spatial discretization

Pseudo-spectral Fourier discretization is a classical method in CFD, for a more complete discussion we refer to [4]. It is a highly accurate method for flows with periodic boundary conditions. In the pseudo-spectral method the vorticity field is transformed to Fourier space in order to compute the spatial derivatives and evolve the vorticity field in time. Terms containing products, i.e. the convection and penalisation terms, are calculated in physical space. The vorticity field and the other variables are represented as truncated Fourier series,

$$\omega(\vec{x}, t) = \sum_{\vec{k} \in \mathbb{Z}^2} \hat{\omega}(\vec{k}, t) \exp(i\vec{k} \cdot \vec{x}) \quad (8)$$

where the Fourier transform of ω is defined as

$$\hat{\omega}(\vec{k}, t) = \frac{1}{4\pi^2} \int \omega(\vec{x}, t) \exp(-i\vec{k} \cdot \vec{x}) d\vec{x} \quad (9)$$

with $\vec{k} = (k_x, k_y)$. The Fourier discretization is uniform in space and is truncated at $k_x = -N_x/2$ and $k_x = N_x/2 + 1$, $k_y = -N_y/2$ and $k_y = N_y/2 + 1$, where N_x and N_y are the number of grid points in x and y direction, respectively. The gradient of ω is computed by multiplication of $\hat{\omega}$ by $i\vec{k}$, the Laplacian by multiplication with $|\vec{k}|^2$. The velocity \vec{u} is computed in Fourier space using Biot–Savart’s law,

$$\vec{u}(\vec{x}, t) = \sum_{\vec{k} \in \mathbb{Z}^2, \vec{k} \neq 0} \frac{i\vec{k}^\perp}{|\vec{k}|^2} \hat{\omega}(\vec{k}, t) \exp(i\vec{k} \cdot \vec{x}) \quad (10)$$

where $\vec{k}^\perp = (-k_y, k_x)$.

The convection term $(\vec{u} + \vec{V}_\infty) \cdot \nabla \omega$ and the penalisation term $\nabla \times (\frac{1}{\eta} \chi_{\Omega_s} \vec{u})$ are evaluated by the pseudo-spectral technique using collocation in physical space. To avoid aliasing errors, i.e. the production of small scales due to the non-linear terms which are not resolved on the grid, we de-alias the vorticity at each time step, by truncating its Fourier coefficients using the 2/3 rule,

$$\hat{\omega}(\vec{k}) = \begin{cases} \hat{\omega}(\vec{k}) & \text{for } \left(\frac{3k_x}{2N_x}\right)^2 + \left(\frac{3k_y}{2N_y}\right)^2 < 1 \\ 0 & \text{for } \left(\frac{3k_x}{2N_x}\right)^2 + \left(\frac{3k_y}{2N_y}\right)^2 \geq 1 \end{cases} \quad (11)$$

For the transformation between physical and Fourier space we use Temperton’s Fast Fourier Transform with an order $N \log_2 N$, ($N = N_x N_y$) complexity [4].

3.2. Adaptive time discretization

For the time discretization we developed a semi-implicit scheme with adaptive time-stepping. The linear diffusion term is discretized implicitly using exact time integration which is cheap for spectral methods, as the Laplace operator is diagonalized in Fourier space, and hence no linear system has to be solved. This improves the stability limit of purely explicit schemes. The remaining terms are discretized explicitly, which avoids the solution of non-linear equations, however it implies a CFL condition on the maximum size of the time step.

3.2.1. Adams–Bashforth scheme

We briefly recall the Adams–Bashforth scheme (see e.g. [21,23] for its application to the Navier–Stokes equations) for initial value problems of the form $dy/dt = f(t, y)$, with $y(t = 0) = y_0$, and present its extension for non-equidistant, i.e. variable, time steps. The general idea of many multi-step methods is to approximate the integral form of the equation,

$$y(t_{p+k}) - y(t_{p-j}) = \int_{t_{p-j}}^{t_{p+k}} f(s, y(s)) ds \quad (12)$$

using an interpolating quadrature rule of the type

$$p_q(s) = \sum_{i=0}^q f(s_{p-i}, y_{p-i}) L_i(s) \quad (13)$$

where L_i denotes the fundamental Lagrange polynomial. This leads to

$$y(t_{p+k}) - y(t_{p-j}) = \Delta t \sum_{i=0}^q \beta_{qi} f(s_{p-i}, y_{p-i}) \quad (14)$$

with a fixed time-step Δt .

For schemes of Adams–Bashforth type we have $k = 1, j = 0$ and $q = 0, 1, 2, \dots$,

$$y_{p+1} = y_p + \Delta t (\beta_{q0} f_p + \beta_{q1} f_{p-1} + \dots + \beta_{qq} f_{p-q}) \quad (15)$$

with $f_p = f(t_p, y_p)$. The coefficients are given by

$$\beta_{qi} = \int_{-j}^k \prod_{l=0, l \neq i}^q \frac{s+l}{-i+l} ds \quad (16)$$

For $q = 0$ we get the classical explicit Euler scheme,

$$y_{p+1} = y_p + \Delta t f_p \quad (17)$$

which is of first order only. For $q = 1$ we obtain the second-order Adams–Bashforth scheme.

$$y_{p+1} = y_p + \frac{3}{2}\Delta t f_p - \frac{1}{2}\Delta t f_{p-1} \tag{18}$$

3.2.2. Extension to variable time steps

Starting with the general formula for the second-order Adams–Bashforth scheme

$$y_{p+1} = y_p + \beta_{11}f_p + \beta_{10}f_{p-1} \tag{19}$$

we develop its extension for variable time steps. In this case the coefficients are given by

$$\beta_{11} = \int_{t_p}^{t_{p+1}} \frac{x - x_{p-1}}{x_p - x_{p-1}} dx = \frac{1}{t_p - t_{p-1}} \left(\frac{1}{2}t_{p+1}^2 - \frac{1}{2}t_p^2 - t_{p-1}(t_{p+1} - t_p) \right) \tag{20}$$

and

$$\beta_{10} = \int_{t_p}^{t_{p+1}} \frac{x - x_p}{x_{p-1} - x_p} dx = \frac{-1}{t_p - t_{p-1}} \left(\frac{1}{2}t_{p+1}^2 - \frac{1}{2}t_p^2 - t_p(t_{p+1} - t_p) \right) \tag{21}$$

where t_p denotes the p th time instant.

Introducing the time step $\Delta t_p = t_p - t_{p-1}$, it follows that

$$\beta_{10} = -\frac{1}{2} \frac{\Delta t_{p+1}}{\Delta t_p} (\Delta t_{p+1} + 2\Delta t_p) \tag{22}$$

and

$$\beta_{11} = -\frac{1}{2} \frac{\Delta t_{p+1}^2}{\Delta t_p} \tag{23}$$

For start-up a first-order scheme is used.

3.3. Fully discretized penalised Navier–Stokes equation

To simplify the notation we rewrite the penalised Navier–Stokes equations (6) in the form of a non-linear evolution equation

$$\partial_t \omega - \nu \nabla^2 \omega = g(\omega) \tag{24}$$

with $g(\omega) = -(\vec{u} + \vec{V}_\infty) \cdot \nabla \omega - \nabla \times (\frac{1}{\eta} \chi_{\Omega_s} \vec{u})$ and where we dropped the index η .

For the exact time integration of the diffusion term we first consider the homogeneous equation, i.e. for $g = 0$. The exact solution is given by

$$\omega(\vec{x}, t) = \omega(\vec{x}, t_0) \exp(\nu t \nabla^2) \tag{25}$$

where $\exp(\nu t \nabla^2)$ is the semi-group of the heat-kernel. As the Laplace operator ∇^2 is diagonal in the Fourier basis, the solution at time step t_{n+1} can be explicitly computed in Fourier space by multiplying the solution at time step t_n with the Fourier transformed heat-kernel

$$\hat{\omega}(\vec{k}, t_{n+1}) = \hat{\omega}(\vec{k}, t_n) \exp(-\nu \Delta t_{n+1} |\vec{k}|^2) \tag{26}$$

where $\Delta t_{n+1} = t_{n+1} - t_n$.

The solution of the inhomogeneous equation, i.e. $g \neq 0$, is given by

$$\omega(\vec{x}, t) = \omega(\vec{x}, t_0) \exp(vt\nabla^2) + \int_{t_0}^t \exp(vs\nabla^2)g(\omega(\vec{x}, t-s)) ds \quad (27)$$

where the Duhamel integral on the right-hand side contains memory effects of the non-linear term. Transforming the above equation into Fourier space, we obtain the following equation to advance the solution in time

$$\hat{\omega}(\vec{k}, t_{n+1}) = \hat{\omega}(\vec{k}, t_n) \exp(-v\Delta t_{n+1}|\vec{k}|^2) + \int_{t_n}^{t_{n+1}} \exp(-vs|k|^2)g(\omega(\vec{x}, \widehat{t_{n+1}} - s)) ds \quad (28)$$

Discretizing the integral with the second-order Adams–Bashforth scheme for adaptive time steps we get the fully discretized equation,

$$\hat{\omega}(\vec{k}, t_{n+1}) = \hat{\omega}(\vec{k}, t_n) \exp(-v\Delta t_{n+1}|\vec{k}|^2) + \quad (29)$$

$$(\beta_{10}g(\omega(\widehat{t_n})) + \beta_{11}g(\omega(\widehat{t_{n-1}}))) \exp(-v\Delta t_n|\vec{k}|^2) \exp(-v\Delta t_{n+1}|\vec{k}|^2) \quad (30)$$

with β_{10} and β_{11} given in Eqs. (22) and (23), respectively.

3.4. Step size control

The step size control of the time step is based on the CFL stability limit of the explicit discretization of the non-linear term. Therefore, in each time step t_n , pointwise the maximal rms velocity is computed:

$$U_{\max} = \max_{\vec{x}} \sqrt{(u(\vec{x}))^2 + (v(\vec{x}))^2} \quad (31)$$

and the new time step is given by

$$\Delta t_{n+1} = C\Delta x/u_{\max}$$

with the minimal spatial grid size $\Delta x = \min\left(\frac{L_x}{N_x}, \frac{L_y}{N_y}\right)$, where L_x, L_y denote the length of the domain in x and y direction, respectively, and $C < 1$ the CFL constant.

4. Numerical results

In this section we apply the presented numerical scheme to study different flow configurations, typically encountered in chemical reactors. We compute the transient flow behaviour in tube bundles, with circular cross sections at $Re = 200$ and 1000 and quadratic cross sections at $Re = 200$, for different angles of attack, i.e. $\alpha = 0^\circ$, corresponding to inline and $\alpha = 30^\circ, 45^\circ$ corresponding to staggered bundles. These configurations are frequently used for cross-flow heat exchangers, because of their ease of construction together with their thermal and mechanical efficiency. We remark that the flow remains largely two-dimensional because of the close packing of the tubes, hence the two-dimensional approximation can be justified [3]. We also compute the transient flow

in a channel with an enclosed cylinder at $Re = 100$ as prototype for a static mixer in a tube reactor. For the different cases we show flow visualizations of instantaneous vorticity fields ω and we plot the time evolution of lift and drag coefficients.

4.1. Tube bundles with circular cross section

In Fig. 1 we sketch the flow configuration for tube bundles with a circular cross section where α is the angle of attack of the free-stream velocity \vec{V}_∞ . The geometry is characterized by the pitch to diameter ratio P/D , where D denotes the tube's diameter and P the tube's pitch. In practical applications the ratio is typically in the range between 1.3 and 2. We define a Reynolds number based on the tube's diameter and the free-stream velocity, i.e. $Re = V_\infty D/\nu$. Prandtl's classical wall law yields for the boundary layer a thickness $\delta \propto 1/\sqrt{Re}$, which thus requires a sufficiently fine grid near the wall.

In the present simulations we are using $D = 1$ and $P = 2$ and $\alpha = 0^\circ, 30^\circ$ and 45° . Note that an angle of attack $\alpha = 0^\circ$ corresponds to an in-line geometry while $\alpha = 45^\circ$ corresponds to a staggered arrangement. In the following we study the transient flow behaviour at two Reynolds-numbers, i.e. $Re = 200$ and 1000 at resolution $N_x = N_y = 256$ and 512 , respectively. This choice guarantees to have at least 4 grid points within the thin boundary layer which ensures that the error in the root mean square drag is less than 2.5%, following [13].

In Fig. 3 we show snapshots of the vorticity field at $t = 10$ for $Re = 200$. For the three different angles on attack we observe a completely different flow behaviour. The inline configuration, i.e. $\alpha = 0^\circ$ (Fig. 3, top, left), exhibits four horizontal shear layers which are stable. The time evolution of the drag and lift coefficient show that the flow becomes after a short transition phase stationary reflected by a constant drag coefficient (Fig. 4, left). The symmetry of the flow is proven by the vanishing lift coefficient. For $\alpha = 30^\circ$ we see much stronger formation of vorticity at the tube's wall. The formed shear layer becomes unstable, is rolling up into vortices which are then shed periodically. This is confirmed by the time evolution of lift and drag coefficients. The staggered geometry with $\alpha = 45^\circ$ also shows a much stronger generation of vorticity compared to the inline case. The shear layer instability leads to the formation of vortices which are subsequently shed

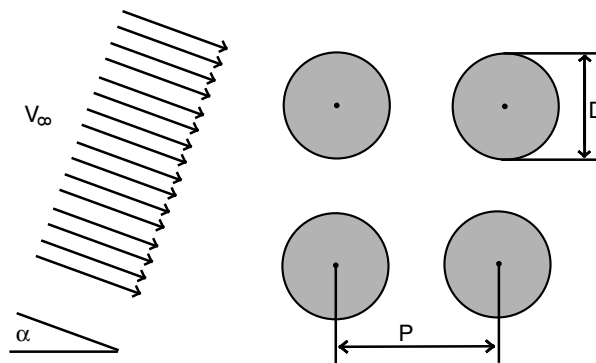


Fig. 1. Sketch of the flow configuration: tube bundles with tube pitch P , tube diameter D and pitch to diameter ratio P/D (which is typically between 1.3 and 2). The angle of incidence is denoted by α .

periodically reflected by the oscillations in the lift and drag coefficients (Fig. 4). Note that the observed Strouhal vortex shedding frequencies between 1.1 and 1.3 agree reasonably well with the reported experimental values of Price et al. [16].

Fig. 5 shows the transient flow regime for the staggered tube bank for $\alpha = 45^\circ$ at $Re = 200$, focussing on one tube only. At early times ($t = 2, 4, 6$) the sequence of vorticity fields shows the formation of two shear layers and the flow exhibits a recirculation region behind the tubes. We can note that the flow regime at $t = 4$ corresponds qualitatively with the flow behaviour observed in experiments, cf. Fig. 2. At later times ($t = 8$) the shear layer becomes unstable and vortices are generated, however, the flow is still symmetric. This is confirmed by the fact that the lift coefficient is still very small (Fig. 4). At $t = 10$ the vortices shed from the tubes, are advected downstream and the flow becomes asymmetric, leading to an increase of the lift coefficient (Fig. 4, right). At $t = 14, 16$ isolated vortices, like in two-dimensional turbulence, are being advected in the inter-tube space with the free-stream and encounter tubes leading to a periodic vortex shedding mechanism.

Increasing the Reynolds number from $Re = 200$ to 1000 the vorticity formation becomes more important, i.e. its magnitude increases. Note that the range of the color table increases from $|\omega| \leq 20$ in Fig. 3 to $|\omega| \leq 100$ in Fig. 6. Furthermore the vorticity is much more localized in space. For the inline geometry ($\alpha = 0^\circ$) we observe now spatial oscillations of the four shear layers without vortex shedding and a pronounced recirculation zone behind the tubes, cf. Fig. 6, top, left. Nevertheless the flow remains symmetric, and therefore the lift coefficient (Fig. 7, left) is vanishing. However, in contrast to the $Re = 200$ case the flow is unsteady.

Changing the angle of incidence to $\alpha = 30^\circ$ (Fig. 6, top, right) we observe the formation of thin boundary layers which are detaching and leading to a vortex shedding. The flow is no more symmetric and well localized vortices are formed, advected and non-linearly interacting in the inter

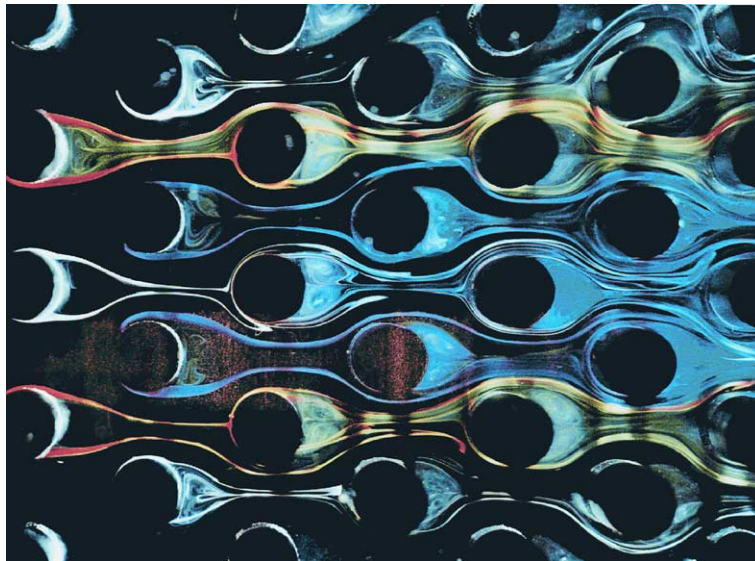


Fig. 2. Flow visualisation of staggered tube bundles for $Re = 200$ and $\alpha = 45^\circ$ (copyright H. Werlé, ONERA, France).

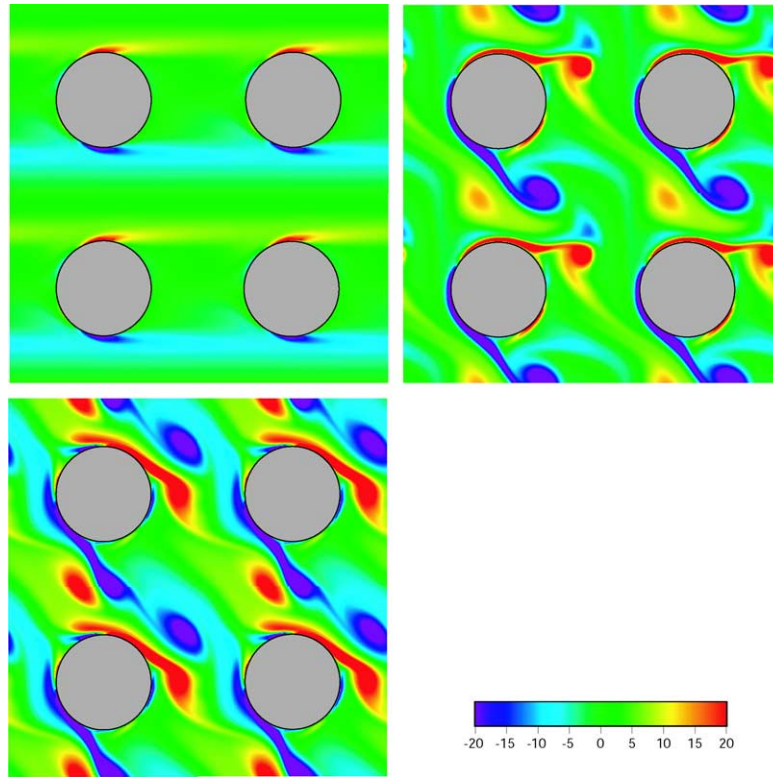


Fig. 3. Flow past tube bundles with circular cross section. Instantaneous vorticity fields at $t = 10$ for three angles of incidence, $\alpha = 0^\circ, 30^\circ, 45^\circ$ at $Re = 200$ with $N_x = N_y = 256$ and $\eta = 10^{-3}$.

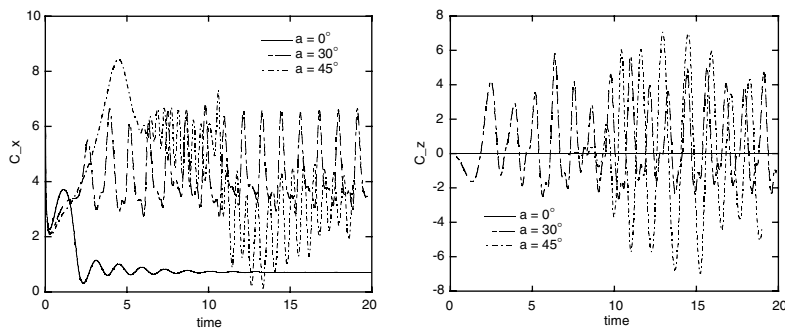


Fig. 4. Flow past tube bundles with circular cross section at $Re = 200$ for $\alpha = 0^\circ, 30^\circ, 45^\circ$. Time evolution of drag (left) and lift (right) coefficients.

tube region. The corresponding lift and drag coefficients (Fig. 7) oscillate in time, however without a clearly pronounced frequency. For the staggered geometry with $\alpha = 45^\circ$ (Fig. 6, bottom, right) the presented snap-shot of the flow is symmetric and well localized co and counter-rotating vor-

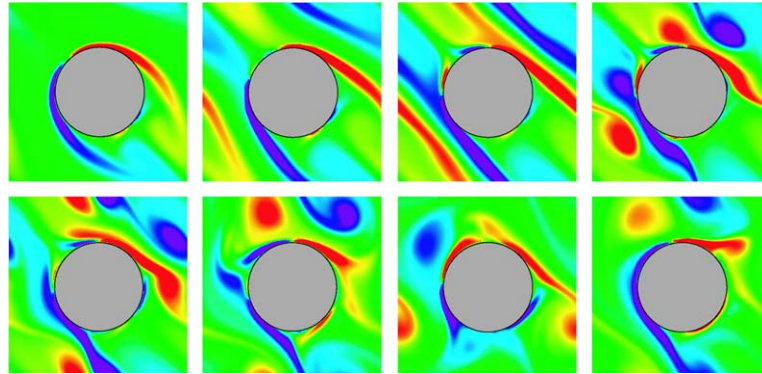


Fig. 5. Flow past staggered tube bundles with circular cross section at $Re = 200$ for $\alpha = 45^\circ$. Time evolution of the vorticity field at $t = 2, 4, 6, 8, 10, 12, 14, 16$.

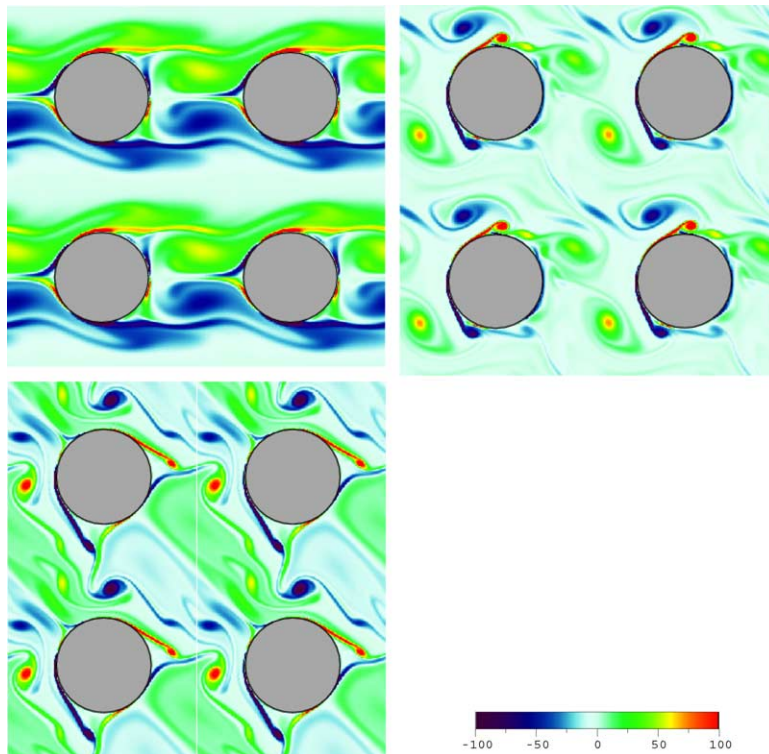


Fig. 6. Flow past tube bundles with circular cross section. Instantaneous vorticity fields at $t = 6$ for three angles of incidence, $\alpha = 0^\circ, 30^\circ, 45^\circ$ at $Re = 1000$ with $N_x = N_y = 512$.

tices are shedding from the tubes. The vanishing lift coefficient is reflecting this symmetry. At later times, around $t = 7$, however, the symmetry is broken and we observe a developing lift force. At the beginning of the simulations the drag forces are continuously increasing up to $t = 5$ and then

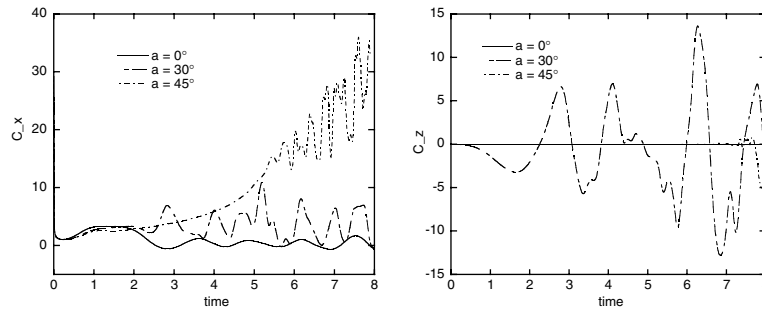


Fig. 7. Flow past tube bundles with circular cross section at $Re = 1000$ for $\alpha = 0^\circ, 30^\circ, 45^\circ$. Time evolution of drag (left) and lift (right) coefficients.

additionally oscillating around a still increasing mean value which becomes stationary around $t = 7$.

4.2. Tube bundles with quadratic cross section

In the following we consider flows past tube bundles with quadratic cross section at $Re = 200$ for three angles of incidence $\alpha = 0^\circ, 30^\circ, 45^\circ$ to compare with the previous case with tubes having a circular cross section. The main difference between both flow configurations is that for quadratic cross sections the detachment point of the boundary layer is well defined at the corner of the tubes while in the circular case it is depending on the Reynolds number and the angle of incidence. We also see that the formation of vorticity is increased by a factor of 4 with respect to the circular case.

For the inline geometry ($\alpha = 0^\circ$) we find in both cases a similar behaviour, again four parallel shear layers are being formed (Fig. 8, top, left), and the flow becomes stationary after a transition phase lasting until $t = 5$. Hence the drag forces are constant and the lift coefficient is vanishing (Fig. 9). The flows in the staggered geometries ($\alpha = 30^\circ, 45^\circ$) exhibit, like for the circular tubes, the formation of vortices which are however less well pronounced (Fig. 8, top, right and bottom, left). For $\alpha = 45^\circ$ we also see the striking symmetry of the flow, which is broken at later times, around $t = 6$ (cf. Fig. 9). In both cases we furthermore observe time oscillations of the drag coefficients, with period $\Delta t = 1$. For $\alpha = 30^\circ$ we also see a superposition of secondary oscillations with period $\Delta t = 0.5$. With respect to the circular tubes we also notice an increase of drag and lift forces by a factor 3.

4.3. Channel flow with cylinder

Finally, we consider a channel flow with obstacle at $Re = 100$, where Re is based on the diameter of the cylinder. This configuration can be seen as a prototype for a static mixer in a tube reactor. Four time instances of vorticity fields at $t = 2.5, 5, 10, 30$ are depicted in Fig. 10. The formed shear layers at the boundary of the cylinder and the channel walls are becoming unstable and vortices are formed which are shed with a clear frequency. The time evolution of the drag and

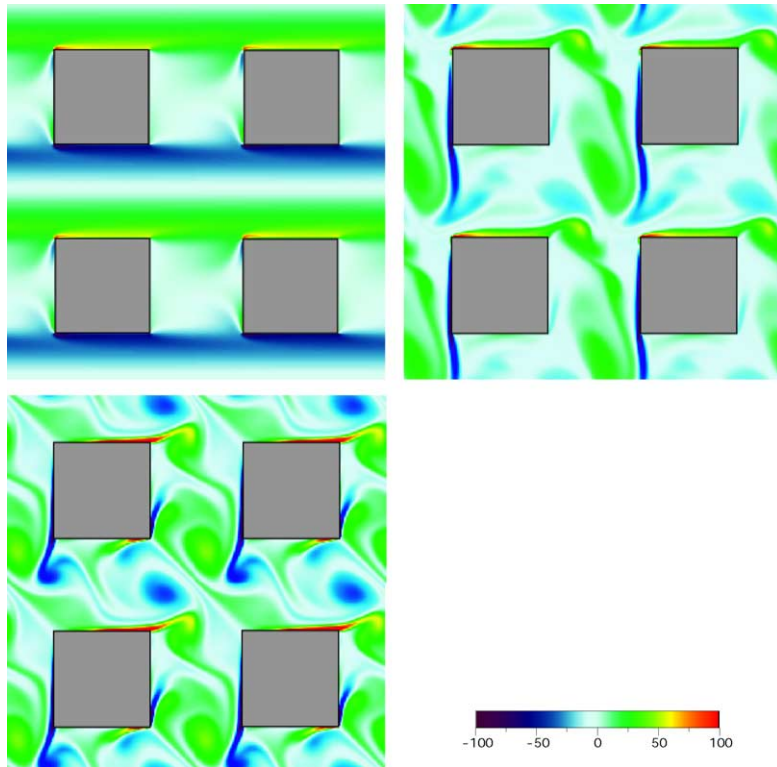


Fig. 8. Flow past tube bundles with quadratic cross section. Instantaneous vorticity fields at $t = 6$ for three angles of incidence, $\alpha = 0^\circ, 30^\circ, 45^\circ$ at $Re = 200$ with $N_x = N_y = 256$ and $\eta = 10^{-3}$.

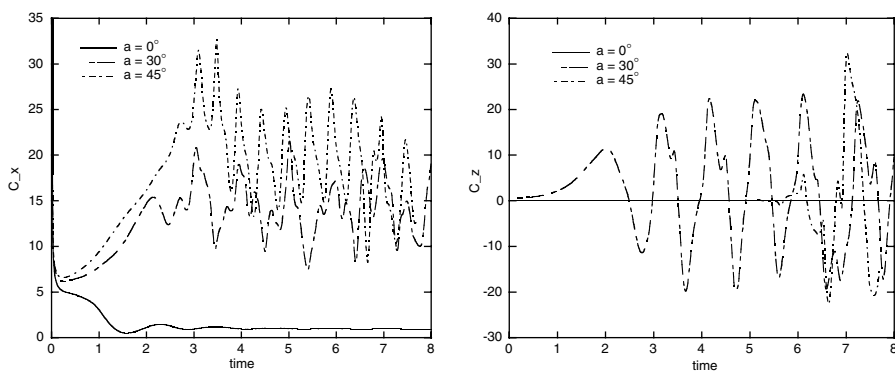


Fig. 9. Flow past tube bundles with quadratic cross section at $Re = 200$ for $\alpha = 0^\circ, 30^\circ, 45^\circ$. Time evolution of drag (left) and lift (right) coefficients.

lift forces (Fig. 11) confirm the oscillation with a clear frequency. The wavelength of the drag oscillations is $\Delta t = 1.4$ corresponding to a frequency of $f = 1/1.4 = 0.7$.

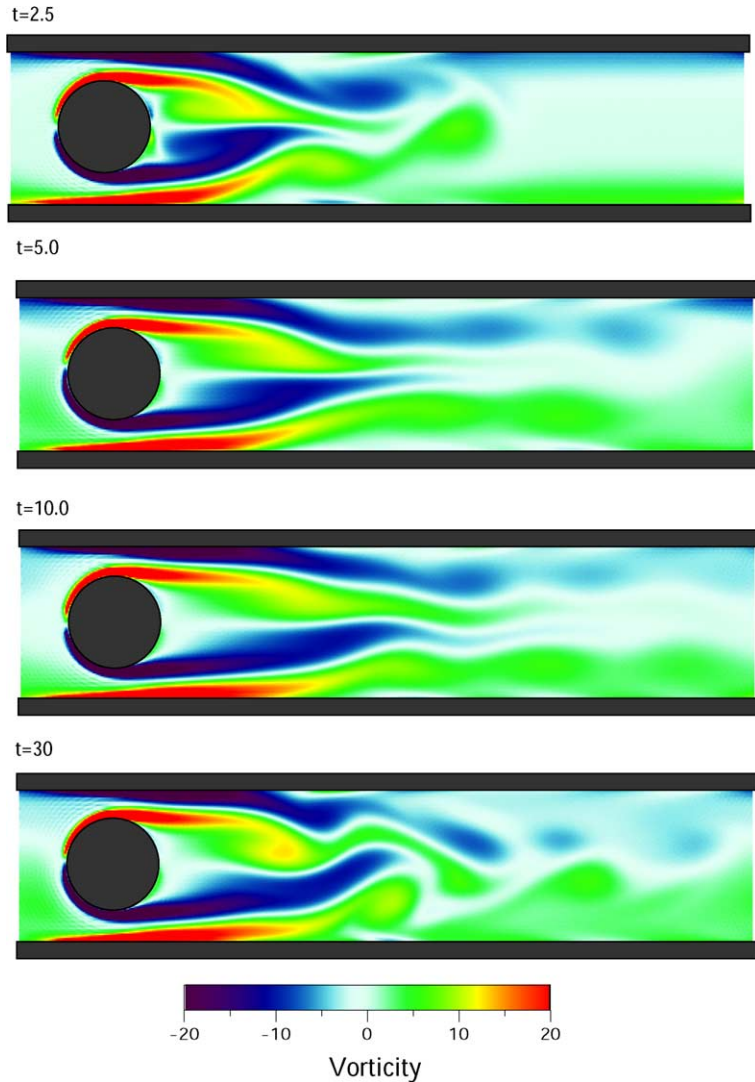


Fig. 10. Channel flow with cylinder at $Re = 100$ with $L_x = 8$, $L_y = 2$ and $N_x = 512$, $N_y = 128$. Vorticity fields at $t = 2.5$, 5, 10, 30.

5. Conclusion

We presented a numerical scheme for computing the time evolution of two-dimensional flows in complex geometries. The utilisation of a penalisation method enables us to take into account complex geometries by a simple mask function without modifying the numerical scheme. The space discretization is based on a high-resolution Fourier pseudo-spectral method which is characterized by its high accuracy, i.e. negligible numerical diffusion and dispersion errors. For the time discretization we presented an adaptive time-stepping scheme based on the exact integration of the linear terms and an Adams–Bashforth discretization of the non-linear terms.

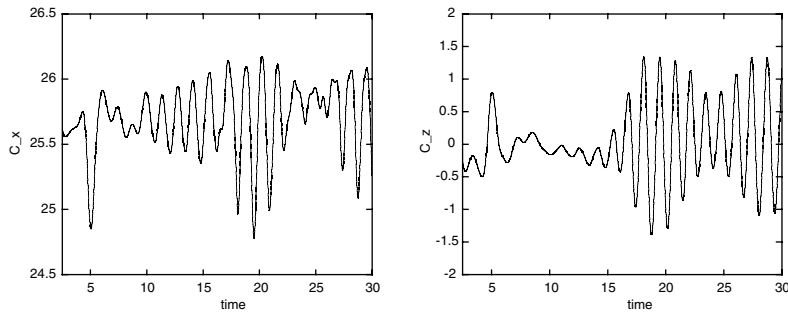


Fig. 11. Channel flow with cylinder at $Re = 100$. Drag (left) and lift (right) coefficients.

We applied the numerical method to different industrially relevant problems, typically encountered in chemical engineering. We studied the transient flow behaviour in tube bundles with circular and quadratic cross sections at different Reynolds numbers and for different angles of attack. The numerical scheme is able to resolve the thin shear layers on the boundary which subsequently become unstable and lead to the formation of co and counter-rotating vortices. Depending on the control parameters we observed strong oscillations of the lift and drag forces which the flow exerts onto the tubes. These may cause damages on the tubes of heat exchanger, especially when their frequency is close to the tubes' resonance frequency.

The two-dimensional approximation of the simulations can be justified due to the dense packing of the tubes. Nevertheless for higher Reynolds numbers, i.e. $Re > 500$ [13] three-dimensional effects become more important and the necessity of detailed three-dimensional studies of the transient behaviour becomes apparent, which is however beyond the scope of this paper.

In [20] we coupled the developed an adaptive wavelet method [9,10,17,18] with the current penalisation approach. This method allows automatic grid generation and refinement around the obstacle and furthermore automatically adapts to the flow evolution. Therewith the number of required grid-points in the simulations can be significantly reduced which permits the computation of high Reynolds number flows.

In future work we will extend the penalisation scheme to three-dimensional flows and perform computations at high Reynolds numbers using the Coherent Vortex Simulation approach, proposed in [5,6].

Acknowledgments

I thank Nicholas Kevlahan for fruitful discussion and for help in developing the numerical code. I also acknowledge partial financial support from the French–German program Procope (contract no. 99090), the European program TMR (contract no. FMRX-CT 98-0184) and the program PPF of ENS Paris (contract no. 15407). Furthermore I am grateful to Henning Bockhorn for all his continuous support during my period at his Institut für Chemische Technik, Universität Karlsruhe, and to Marie Farge for bringing to my knowledge the penalisation method.

References

- [1] Angot P, Bruneau C-H, Fabrice P. A penalisation method to take into account obstacles in viscous flows. *Numer Math* 1999;81:497–520.
- [2] Arquis E, Caltagirone JP. Sur les conditions hydrodynamiques au voisinage d'une interface milieu fluide—milieu poreux: application à la convection naturelle. *CR Acad Sci Paris II* 1984;299:1–4.
- [3] Beale SB, Spalding DB. A numerical study of unsteady flow in in-line and staggered tube banks. *J Fluid Struct* 1999;13:723–54.
- [4] Canuto C, Hussaini MY, Quaternioni A, Zang TA. *Spectral methods in fluid dynamics*. Berlin: Springer-Verlag; 1988.
- [5] Farge M, Schneider K, Kevlahan N. Non-Gaussianity and coherent vortex simulation for two-dimensional turbulence using an adaptive orthonormal wavelet basis. *Phys Fluids* 1999;11(8):2187–201.
- [6] Farge M, Schneider K. Coherent vortex simulation (CVS), a semi-deterministic turbulence model using wavelets. *Flow, Turbul Combust* 2001;66(4):393–426.
- [7] Ferziger J, Peric M. *Numerical methods in fluid dynamics*. Berlin: Springer-Verlag; 1996.
- [8] Forestier M, Pasquetti R, Peyret R. Calculations of 3D wakes in stratified fluids. In: *ECCOMAS*; 2000.
- [9] Fröhlich J, Schneider K. Numerical simulation of decaying turbulence in an adaptive wavelet basis. *Appl Comput Harm Anal* 1996;3:393–7.
- [10] Fröhlich J, Schneider K. An adaptive wavelet–vaguelette algorithm for the solution of PDEs. *J Comput Phys* 1997;130:174–90.
- [11] Glowinsky R, Pan TW, Wells Jr RO, Zhou X. Wavelet and finite element solutions for the Neumann problem using fictitious domains. *J Comput Phys* 1996;126:40–51.
- [12] Goldstein D, Handler R, Sirovich L. Modeling no-slip flow boundary with an external force field. *J Comput Phys* 1993;105:354–66.
- [13] Kevlahan N, Ghidaglia J-M. Computation of turbulent flow past an array of cylinders using a spectral method with Brinkman penalization. *Eur J Mech/B* 2001;20:333–50.
- [14] Khadra K, Parneix S, Angot P, Caltagirone J-P. Fictitious domain approach for numerical modelling of Navier–Stokes equations. *Int J Num Meth Fluids* 2000;34:651–84.
- [15] Peskin CS. The immersed boundary method. *Acta Numer* 2002:479–517.
- [16] Price SJ, Paidoussis MP, Mark B. Flow visualization of the interstitial cross-flow through parallel triangular and rotated square arrays of cylinders. *J Sound Vibr* 1995;181(1):85–98.
- [17] Schneider K, Kevlahan N, Farge M. Comparison of an adaptive wavelet method and nonlinearly filtered pseudo-spectral methods for two-dimensional turbulence. *Theor Comput Fluid Dyn* 1997;9(3/4):191–206.
- [18] Schneider K, Farge M. Wavelet approach for modelling and computing turbulence. In: *Lecture series 1998–05 advances in turbulence modelling*. Bruxelles: von Karman Institute for Fluid Dynamics; 1998. 132 p.
- [19] Schneider K. *Modélisation et simulation numérique en base d'ondelettes adaptative: applications en mécanique des fluides et en combustion*. Habilitation thesis. Université Louis Pasteur Strasbourg, 2001.
- [20] Schneider K, Farge M. Adaptive wavelet simulation of a flow around an impulsively started cylinder using penalisation. *Appl Comput Harm Anal* 2002;12:374–80.
- [21] Stoer J, Bulirsch R. *Einführung in die Numerische Mathematik II*, Heidelberg Taschenbücher. New York: Springer; 1978.
- [22] Tseng Y-H, Ferziger J. A ghost-cell immersed boundary method for flow in complex geometry. *J Comput Phys* 2003;192:593–623.
- [23] Vanel J-M, Peyret R, Bontoux P. A pseudo-spectral solution of vorticity–streamfunction equations using the influence matrix technique. In: Morton KW, Baines MJ, editors. *Numerical methods for fluid dynamics*. Oxford: Clarendon Press; 1986. p. 477–88.